*Journal of Advanced Ceramics*
2022, **11**(12): 1918–1931
https://doi.org/10.1007/s40145-022-0656-5

ISSN 2226-4108
CN 10-1154/TQ

**Research Article**

# Mechanical properties of additively-manufactured cellular ceramic structures: A comprehensive study

Xueqin ZHANG[a], Keqiang ZHANG[a], Bin ZHANG[b], Ying LI[a,*], Rujie HE[a,*]

[a]*Institute of Advanced Structure Technology*, *Beijing Institute of Technology*, *Beijing 100081*, *China*
[b]*School of Naval Architecture*, *Ocean and Energy Power Engineering*, *Wuhan University of Technology*, *Wuhan 430070*, *China*

Received: May 13, 2022; Revised: August 25, 2022; Accepted: September 19, 2022


**Abstract:** Cellular ceramic structures (CCSs) are promising candidates for structural components in aerospace and modern industry because of their extraordinary physical and chemical properties. Herein, the CCSs with different structural parameters, i.e., relative density, layer, size of unit cells, and structural configuration, were designed and prepared by digital light processing (DLP)-based additive manufacturing (AM) technology to investigate their responses under compressive loading systematically. It was demonstrated that as the relative density increased and the size of the unit cells decreased, the mechanical properties of one-layer CCSs increased. The mechanical properties of three-layer CCSs were more outstanding than those of the CCSs with one and two layers. In addition, structural configurations also played a vital role in the mechanical properties of the CCSs. Overall, the mechanical properties of the CCSs from superior to inferior were that with the structural configurations of modified body-centered cubic (MBCC), Octet, SchwarzP, IWP, and body-centered cubic (BCC). Furthermore, structural parameters also had significant impacts on the failure mode of the CCSs under compressive loading. As the relative density increased, the failure mode of the one-layer CCSs changed from parallel–vertical–inclined mode to parallel–vertical mode. It was worth noting that the size of the unit cells did not alter the failure mode. Inclined fracture took a greater proportion in the failure mode of the multi-layer CCSs. But it could be suppressed by the increased relative density. Similarly, the proportions of the parallel–vertical mode and the fracture along a specific plane always changed with the variation of the structural configurations. This study will serve as the base for investigating the mechanical properties of the CCSs.

**Keywords:** cellular ceramic structures (CCSs); mechanical properties; failure mode; structural parameters

## 1 Introduction

Mass reduction and load bearing are always critical drivers for structural components in aerospace and modern industry [1,2]. The emergence of cellular structures, which contain cellular polymer structures (CPSs), cellular metal structures (CMSs), and cellular ceramic structures (CCSs), makes the load-bearing but lightweight structural components a reality [3–8]. Because the cellular structures are able to decrease the mass without compromising the mechanical properties

* Corresponding authors.
E-mail: Y. Li, bitliying@bit.edu.cn;
R. He, herujie@bit.edu.cn

of components per unit mass. On the one hand, the combination of characteristics of superior strength, extraordinary high-temperature resistance, and undisputed low density of the CCSs make them promising candidates for aerospace and modern industry. On the other hand, the subsequent development of additive manufacturing (AM) technologies makes the CCS a topic of growing concern and research [9–15].

The CCSs refer to the ceramic components composed of periodical unit cells with tailored structural parameters arranged in a three-dimensional space. The unit cells are usually divided into lattices, triply periodic minimal surfaces (TPMS), and mixed cells based on the structural configurations [1]. Numerous works have been deployed to explore the mechanical properties of the CCSs. Mei *et al*. [16] proved that the mechanical properties of $Al_2O_3$ CCSs depended on their structural configurations. The $Al_2O_3$ CCSs with an Octet structure, i.e., a typical stretching-dominant structure, performed more extraordinary load-bearing capacity than that with a representative bending-dominant body-centered cubic (BCC) structure. Not only compressive responses but also flexural performances of the CCSs were significantly influenced by the structural configurations [17]. Zhao *et al*. [18] clearly testified that the flexural strength of additively manufactured $ZrO_2$ with a Kelvin structural configuration was more excellent than that with the Octet structural configuration. The TPMS is further adapted to the CCSs, aiming to alleviate the stress concentrated on the joint of struts and increase their mechanical properties. Interestingly, mixing the diverse unit cells into the CCS made it exhibit a hybrid failure mode concerning fracture path and orientation under compressive loading [19]. Besides, no matter whether the structural configuration was P-cell or Neovius, Shen *et al*. [20] testified that stress–strain curves of the CCSs got upside as the numbers of the unit cells in the $x$, $y$, or $z$ axis increased. Furthermore, it had been extensively illustrated that the mechanical properties, i.e., compressive strength, flexural strength, and Young's modulus, were significantly impacted by the relative density. With the increase of the relative density, the mechanical properties of the CCSs got close to those of additively-manufactured dense ceramics at an exponential rate [21,22]. Besides, the size of the unit cells needs to be considered when studying the CCSs. Zhao *et al*. [23] fabricated the CCSs with the same Octet structural configuration but different sizes of the unit cells. It was revealed that the compressive strength of the CCSs increased from ~10 to ~70 MPa as the unit cell decreased from 10 mm × 10 mm × 10 mm to 2 mm × 2 mm × 2 mm. All these works testified that the mechanical properties of the CCSs could be tailored by the structural parameters. Furthermore, the failure mode of the CCSs was simultaneously revealed when investigating the mechanical properties. Lu *et al*. [24] and Shuai *et al*. [25] primarily analyzed the stress distributions in the unit cells and whole CCSs under the compressive loading in the elastic range, respectively, demonstrating the stress concentrated on the joints and somewhere parallel to the loading direction. Zhang *et al*. [26] and Mei *et al*. [16] illustrated that the crush of the $Al_2O_3$ CCSs always happened on the joints located at a specific plane.

Plentiful works and splendid achievements of the mechanical properties of the CCSs have been deployed and harvested with the endeavor of research. However, the additively manufactured CCSs remained far from applications. Because most work, which had been extensively carried out, just focused on how one or two structural parameters influence the mechanical properties of the CCSs. In fact, the effects of the structural parameters are not isolated. Those are always influenced by each other.

Herein, the responses of digital light processing (DLP)-based additively manufactured $Al_2O_3$ CCSs under the compressive loading were characterized systematically. Firstly, the CCSs with different relative densities, layers, sizes, and structural configurations were designed and fabricated by the DLP-based AM technology. The mechanical properties and failure modes of the CCSs were investigated entirely. Most importantly, we comprehensively concluded a particular radar map to evaluate the effect of the structural parameters on the CCSs. This study provides a database to systematically tailor the mechanical properties of the CCSs based on the obtained results, accelerating the successful development of programmable CCSs.

## 2 Materials and methods

### 2. 1 Structure design

The CCSs with different structural parameters (relative density, layer, size, and structural configuration) are designed to reveal the influence of the structural parameters on the mechanical properties of the CCSs.

Five structural configurations with a 40% relative density are introduced in Group D to investigate the

influence of the structural configuration on the mechanical properties of the CCSs. The relative density refers to the volume ratio of the CCSs occupied in a cube with the same length, width, and height. As listed in Table 1, the unit cells of the CCSs with a 6 mm × 6 mm × 6 mm size are arranged in a 5 × 5 × 5 array. Among five structural configurations, the BCC, of course, is the most familiar and typical bending-dominated structural configuration originating from the arrangement mode of atoms. The modified body-centered cubic (MBCC) is created based on the BCC by dividing BCC into two parts along the central plane and the overlapping two parts with each other in height. The Octet is the most typical stretching-dominated

**Table 1 Dimension parameters of CCS's unit cell**

| Group | No. | Array | | Relative density | Length | | Width | | Height | | Diameter | |
|---|---|---|---|---|---|---|---|---|---|---|---|---|
| | | | | | Dimens. (mm) | SCR (%) | Dimens. (mm) | SCR (%) | Dimens. (mm) | SCR (%) | Dimens. (mm) | SCR (%) |
| O | O15 | 3 × 3 × 1 | Des. | 15% | 10.00 | 18.70 | 10.00 | 20.20 | 7.07 | 20.93 | 1.44 | 15.97 |
| | | | Meas. | 15.6% | 8.13 | | 7.98 | | 5.59 | | 1.21 | |
| | O25 | 3 × 3 × 1 | Des. | 25% | 10.00 | 19.50 | 10.00 | 20.70 | 7.07 | 21.07 | 1.92 | 16.15 |
| | | | Meas. | 25.2% | 8.05 | | 7.93 | | 5.58 | | 1.61 | |
| | O35 | 3 × 3 × 1 | Des. | 35% | 10.00 | 19.20 | 10.00 | 20.20 | 7.07 | 21.50 | 2.36 | 18.64 |
| | | | Meas. | 35.6% | 8.08 | | 7.98 | | 5.55 | | 1.92 | |
| T | T15 | 3 × 3 × 2 | Des. | 15% | 10.00 | 19.00 | 10.00 | 19.20 | 7.07 | 22.21 | 1.44 | 15.28 |
| | | | Meas. | 14.9% | 8.10 | | 8.08 | | 5.50 | | 1.22 | |
| | T25 | 3 × 3 × 2 | Des. | 25% | 10.00 | 19.80 | 10.00 | 20.00 | 7.07 | 21.92 | 1.92 | 16.15 |
| | | | Meas. | 25.3% | 8.02 | | 8.00 | | 5.52 | | 1.61 | |
| | T35 | 3 × 3 × 2 | Des. | 35% | 10.00 | 19.60 | 10.00 | 20.10 | 7.07 | 24.05 | 2.36 | 20.76 |
| | | | Meas. | 34.6% | 8.04 | | 7.99 | | 5.37 | | 1.87 | |
| TH | TH15 | 3 × 3 × 3 | Des. | 15% | 10.00 | 18.50 | 10.00 | 19.50 | 7.07 | 22.77 | 1.44 | 16.67 |
| | | | Meas. | 15.7% | 8.15 | | 8.05 | | 5.46 | | 1.20 | |
| | TH25 | 3 × 3 × 3 | Des. | 25% | 10.00 | 19.60 | 10.00 | 22.70 | 7.07 | 23.01 | 1.92 | 16.15 |
| | | | Meas. | 25.8% | 8.04 | | 7.73 | | 5.44 | | 1.61 | |
| | TH35 | 3 × 3 × 3 | Des. | 35% | 10.00 | 19.80 | 10.00 | 20.60 | 7.07 | 23.06 | 2.36 | 20.34 |
| | | | Meas. | 35.6% | 8.02 | | 7.94 | | 5.44 | | 1.88 | |
| H | H15 | 3 × 3 × 1 | Des. | 15% | 7.78 | 19.02 | 7.78 | 20.05 | 5.5 | 20.36 | 1.12 | 19.64 |
| | | | Meas. | 16.1% | 6.30 | | 6.22 | | 4.38 | | 0.90 | |
| | H25 | 3 × 3 × 1 | Des. | 25% | 7.78 | 19.54 | 7.78 | 20.44 | 5.5 | 20.18 | 1.50 | 17.33 |
| | | | Meas. | 26.3% | 6.26 | | 6.19 | | 4.39 | | 1.24 | |
| | H35 | 3 × 3 × 1 | Des. | 35% | 7.78 | 18.89 | 7.78 | 20.18 | 5.5 | 22.00 | 1.84 | 18.48 |
| | | | Meas. | 25.8% | 6.31 | | 6.21 | | 4.29 | | 1.50 | |
| D | BCC40 | 5 × 5 × 5 | Des. | 40% | 6.00 | 20.67 | 6.00 | 23.17 | 6.00 | 21.00 | 1.93 | 20.21 |
| | | | Meas. | 38.9% | 4.76 | | 4.61 | | 4.74 | | 1.54 | |
| | Octet40 | 5 × 5 × 5 | Des. | 40% | 6.00 | 20.17 | 6.00 | 22.17 | 6.00 | 21.00 | 1.24 | 18.55 |
| | | | Meas. | 41.4% | 4.79 | | 4.67 | | 4.74 | | 1.01 | |
| | MBCC 40 | 5 × 5 × 5 | Des. | 40% | 6.00 | 19.83 | 6.00 | 22.83 | 6.00 | 20.33 | 1.65 | 19.39 |
| | | | Meas. | 41.0% | 4.81 | | 4.63 | | 4.78 | | 1.33 | |
| | Schwarz P40 | 5 × 5 × 5 | Des. | 40% | 6.00 | 19.50 | 6.00 | 19.67 | 6.00 | 23.17 | — | — |
| | | | Meas. | 39.4% | 4.83 | | 4.82 | | 4.61 | | | |
| | IWP40 | 5 × 5 × 5 | Des. | 40% | 6.00 | 20.17 | 6.00 | 20.17 | 6.00 | 22.33 | — | — |
| | | | Meas. | 42.6% | 4.79 | | 4.79 | | 4.66 | | | |

Note: SCR is the abbreviation of sintering contraction ratio; Des. and Meas. mean designed and measured, respectively; Dimens. means dimension.

structure. The models of the SchwarzP and IWP are established by Eqs. (1) [27] and (2) [28], respectively:

$$\cos kx + \cos ky + \cos kz = 0 \quad (1)$$

$$(\cos kx \cos ky + \cos ky \cos kz + \cos kz \cos kx) - (\cos 2kx + \cos 2ky + \cos 2kz) = 0 \quad (2)$$

where $k$ is the constant determining the relative density of the CCSs.

The structural configurations of the CCSs involved in other groups are the MBCC. As described in Table 1, the length, width, and height of the as-designed unit cells in Group O are fixed at 10, 10, and 7.07 mm, respectively. The unit cells are repeatedly arranged three, three, and one times in the $x$, $y$, and $z$ axes to generate the CCSs in Group O, respectively. The relative densities of O15, O25, and O35 are 15%, 25%, and 35%, respectively, to discover the effect of the relative density. The only difference between the CCSs in Group O, Group T, and Group TH is the layers. There are one, two, and three layers of the unit cells in the CCSs in Group O, Group T, and Group TH, respectively, which are used to explore the effect of the layers. The CCSs in Group H are obtained by shrinking the CCSs in Group O to 77.8%, which is used to investigate the mechanical properties of the CCSs with different sizes of the unit cells.

### 2. 2 Fabrication

The CCSs were fabricated from an $Al_2O_3$ photosensitive slurry by a DLP system (AutoCera, Beijing 10 Dimensions Science and Technology Co., Ltd., China). The photosensitive slurry comprised $Al_2O_3$ coarse powders, $Al_2O_3$ fine powders, photosensitive resin monomers, photoinitiators, dispersants, and sintering aids. Detailed information about the slurry was listed in Ref. [29]. The exposure density and time of ultraviolet light were set as 12,000 μW/cm$^2$ and 4 s, respectively. The as-designed models of the targets were sliced at a thickness of 100 μm. After the DLP, the as-accomplished green bodies were immersed in ethanol to a clean redundant slurry. The subsequent debinding and sintering of dried green bodies were executed at 550 ℃ (heating rate = 1 ℃/min) and 1650 ℃ (heating rate = 5 ℃/min) in muffle furnaces (FMJ-07/11 and FMJ-05/17, respectively, HeFei Facerom Thermal Equipment Co., Ltd., China) to obtain final products. The atmosphere in muffle furnaces was air. It has been measured that the forming accuracy of the DLP system reaches as high as 99.5%, meeting the requirement. Besides, the porosity and density of additively manufactured bulk $Al_2O_3$ are 7.03% and 3.70 g/cm$^3$, respectively. Its compressive strength and flexural strength are 523.6 and 178.84 MPa, respectively [30].

### 2. 3 Characterization and testing

The dimensions of the CCSs were manually measured by a digital micrometer (211-101, Anyi Instrument Co., Ltd., China). A scanning electron microscope (SEM; EVO18, ZEISS, Germany) operated at an accelerating voltage of 5 kV was used to observe the micro-morphologies of the CCSs. The mechanical properties of the CCSs were examined by a universal testing machine (LD 23, Shenzhen Labsans Testing Machine Co., Ltd., China). Loading speed was set as 0.2 mm/min. To alleviate friction, Teflon films were placed between the tested CCSs and pressure heads. Three specimens were repeatedly tested to verify the reliability.

## 3 Results and discussion

### 3. 1 Morphology of CCSs

The macro- and micro-morphologies of the MBCC CCSs in Group O, Group T, and Group TH are displayed in Fig. 1. It was observed that the macro-morphology of every CCS was in accord with the as-designed model. The diameters of the struts in the CCSs got thicker as the relative density increased. What was different from the established models, on the one hand, was the surface morphology of the CCSs. As depicted in Fig. 1, apparent step-wise morphology, rather than a continuously smooth surface as designed, could be observed on the surface of the struts. Such discrimination was attributed to the layer-by-layer forming characteristic of the DLP technology, which may deteriorate the mechanical properties of the CCSs to some extent [31]. Luckily, the step-wise morphology depended on the inclination angle of the struts. Apart from the CCSs in Group D, the inclination angle of every MBCC CCS was 45°. Hence, the effect of the step-wise morphology on the mechanical properties of the CCSs was not taken into consideration in the analysis. On the other hand, as listed in Table 1, the dimension parameters of the CCSs significantly deviated from that of the as-designed models. Apparent contraction happened during the sintering process. Such contraction was caused by the removal

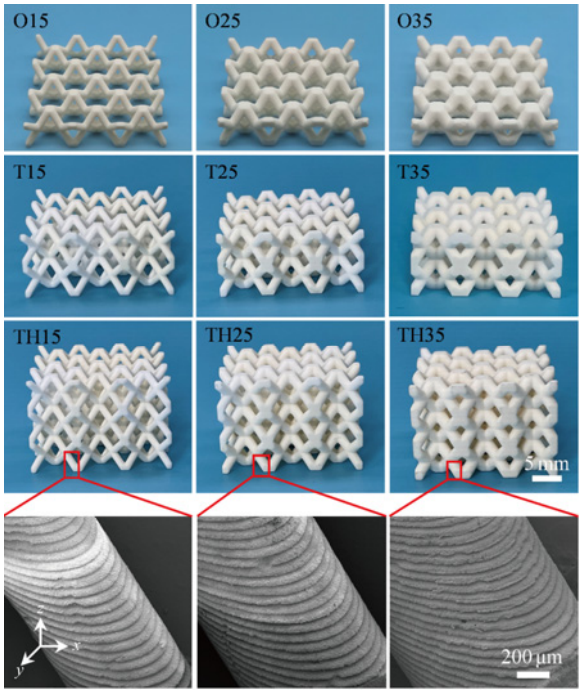


**Fig. 1** Macro- and micro-morphologies of MBCC CCSs with different relative densities and layers.

of resins and densification of $Al_2O_3$ powders in the sintering process [32]. Besides, due to the inhomogeneous distributions of ultraviolet light in the $x$ and $y$ axes, the as-printed green bodies embodied the diverse dimensions in the $x$ and $y$ axes, leading to different SCRs. Significantly, the SCR was slightly higher in the $z$ axis on the whole, which was attributed to the more extensive solidified resins in the $z$ axis. In brief, the dimension of the CCSs could be preciously controlled based on the calculated dimensions and corresponding SCRs.

Furthermore, the one-layer CCSs belonging to Group H are shown in Fig. 2(a). The effect of unit cell size on the mechanical properties and failure mode of the CCSs was revealed by comparing the performance of the CCSs in Group H and Group O. The multi-layer CCSs in Group D with the BCC, Octet, MBCC, SchwarzP, and IWP structures and a 40% relative density are also presented in Fig. 2(b) to investigate how the structural configurations influenced the response of the CCSs under the compressive loading.

### 3.2 Effect of relative density

The compression test was conducted on the MBCC CCSs belonging to Group O, Group T, and Group TH to examine how their mechanical properties changed along with the relative density. Typical stress–strain curves of the MBCC CCSs are plotted in Fig. 3. The exhibited stress and strain are calculated based on the detected force and displacement. It can be seen in Fig. 3

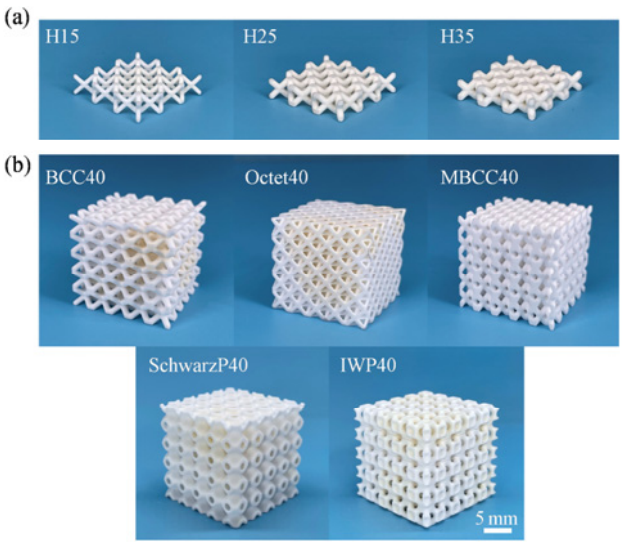


**Fig. 2** Macro-morphologies of CCSs belonging to (a) Group H and (b) Group D.

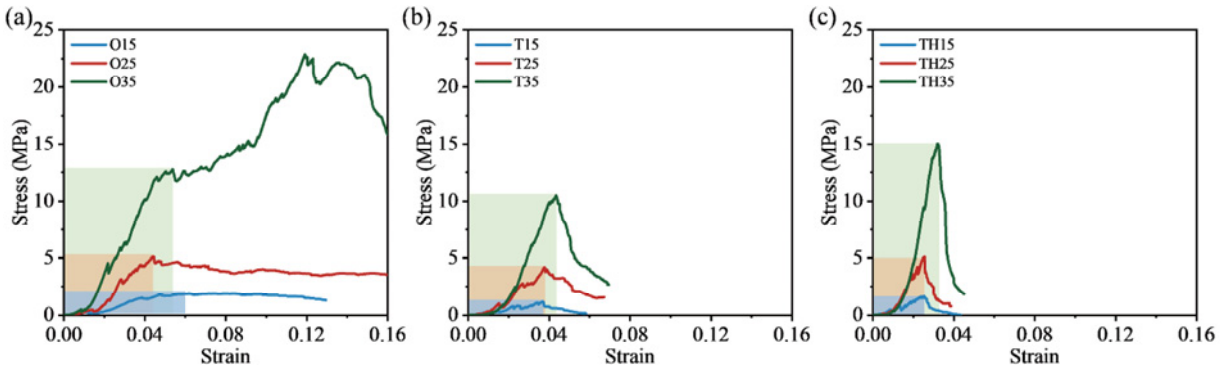


**Fig. 3** Representative compressive stress–strain curves of MBCC CCSs with different layers: (a) one layer, (b) two layers, and (c) three layers.

that, most stress–strain curves exhibited a similar variation tendency, i.e., the stress linearly increased with the oscillation at the initial stage (marked by colorful cubes). The initial loading stage before the stress climbing to the highest value was defined as a linear elastic stage based on the characteristic of the stress–strain curve of the CCSs. It was worth noticing that not only elastic deformation but also inelastic deformation happened in the defined linear elastic stage. That is to say, although the MBCC CCSs were destroyed partially, they were still capable of bearing the increased loading. As the test went on, the stress reached the maximum. At the maximum, the MBCC CCSs had been completely destroyed and would not provide support anymore. Hence, the stress–strain curves of most of MBCC CCSs decreased at the end of the linear elastic stage. For example, the stress–strain curve of TH35 dramatically declined as the stress climbed to the maximum value of 14.96 MPa. Significantly, something different happened on O35. The stress–strain curve of O35 still increased after reaching the first maximum value of 12.58 MPa instead of declining immediately. It just began to decrease at a strain of 0.12 with a stress of 22.76 MPa. Such difference was ascribed to the geometric effect resulting from the height–width ratio of the MBCC CCSs [21]. When examining the load-bearing capacity of O35, the room between the upper and lower pressure heads was too narrow to accommodate the position adjustment of broken struts. The broken struts of O35 would get overlapped with each other. The broken O35 continued to provide support in the following test. On the whole, the stress–strain curves went upward as the relative density increased, which was not changed by the layers of the MBCC CCSs. That is to say, increasing the relative density could significantly increase the load-bearing capacity of the MBCC CCSs.

In order to quantitatively analyze the mechanical properties of the MBCC CCSs, the compressive strength, Young's modulus, energy absorption, and strain extracted from Fig. 3 are demonstrated in Figs. 4(a), 4(b), 4(c), and 4(g), respectively. Here, the compressive strength of the MBCC CCSs was defined as the max stress in the stress–strain curves apart from O35, whose compressive strength was the first max strength. The Young's modulus was the slope of the stress–strain curves in the linear elastic stage. The strain used here was equivalent strain, i.e., the variation of the strain in the linear stage of the stress–strain curves. The energy absorption referred to the energy that the MBCC CCSs absorbed before the stress got max, which was represented by the area under the stress–strain curves from the start to the strain corresponding to the max stress.

It is concluded from Fig. 4 that, when the layer of the MBCC CCSs was one, all compressive strength, Young's modulus, and energy absorption obviously increased with the increase of the relative density. Similarly, the compressive strength, Young's modulus, and energy absorption of the MBCC CCSs with two and three layers also increased as the relative density increased. As listed in Table 1, the increased relative density of the MBCC CCSs was achieved by the increased diameter of the struts in the MBCC CCSs, which further led to the enhanced compressive strength and Young's modulus. It seems that the strains were not influenced by the relative density, as depicted in Fig. 4(g). Because the equivalent strain of the MBCC CCSs contained their elastic deformation in elastic limit and inelastic deformation from the position change of the broken struts. The inelastic deformation of the broken struts dominated the strain of the MBCC CCSs, which was related to the layers but not influenced by the relative density. Hence, the strains were scarcely influenced by the increased relative density. There was no doubt that the area covered by the stress–strain curves and the $x$ axis was dependent on the stress and strain. Under the comprehensive function of the increased compressive strength and less invariable strain, the energy absorption of the MBCC CCSs similarly kept incremental along with the increased relative density. Furthermore, as listed in Eqs. (3)–(5), the relationships between the relative density and the compressive strength, Young's modulus, and energy absorption obeyed the exponential law [21].

$$\begin{cases} S_{\mathrm{O}} = (135.32 \pm 26.44)\bar{\rho}^{2.37\pm0.18} \\ S_{\mathrm{T}} = (318.50 \pm 60.95)\bar{\rho}^{3.08\pm0.17} \\ S_{\mathrm{TH}} = (575.48 \pm 182.55)\bar{\rho}^{3.54\pm0.29} \end{cases} \tag{3}$$

$$\begin{cases} Y_{\mathrm{O}} = (9.35 \pm 0.50)\bar{\rho}^{3.04\pm0.49} \\ Y_{\mathrm{T}} = (15.95 \pm 3.62)\bar{\rho}^{3.37\pm0.20} \\ Y_{\mathrm{TH}} = (33.23 \pm 15.26)\bar{\rho}^{3.64\pm0.42} \end{cases} \tag{4}$$

$$\begin{cases} E_{\mathrm{O}} = (1.77 \pm 0.50)\bar{\rho}^{2.10\pm0.25} \\ E_{\mathrm{T}} = (8.20 \pm 4.04)\bar{\rho}^{3.61\pm0.44} \\ E_{\mathrm{TH}} = (7.64 \pm 2.33)\bar{\rho}^{3.80\pm0.28} \end{cases} \tag{5}$$

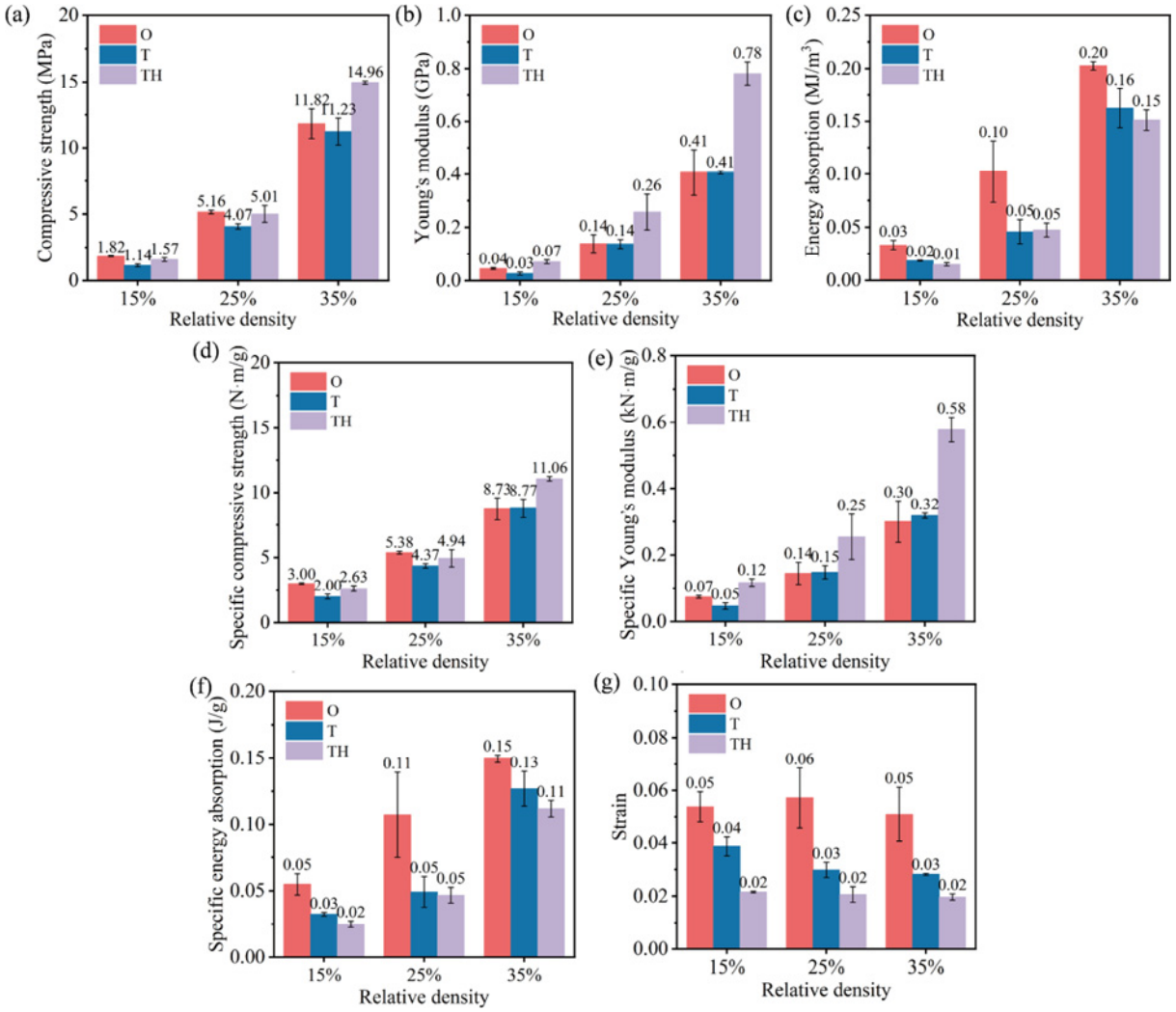


**Fig. 4** Summarization of mechanical properties of MBCC CCSs in Group O, Group T, and Group TH: (a) compressive strength, (b) Young's modulus, (c) energy absorption, (d) specific compressive strength, (e) specific Young's modulus, (f) specific energy absorption, and (g) strain.

where $\overline{\rho}$ is the relative density of the CCSs; $S_O$, $S_T$, and $S_{TH}$ are the compressive strengths of the CCSs with one, two, and three layers, respectively; $Y_O$, $Y_T$, and $Y_{TH}$ represent the Young's moduli of the CCSs with one, two, and three layers, respectively. Likely, the energy absorption of the CCSs with one, two, and three layers are represented by $E_O$, $E_T$, and $E_{TH}$, respectively.

Specific mechanical properties of the MBCC CCSs were further taken into consideration to measure the lightweight efficiency and load-bearing capacity simultaneously. Specific compressive strength, specific Young's modulus, and specific energy absorption are calculated and exhibited in Figs. 4(d), 4(e), and 4(f), respectively. It was clearly observed that although the gaps among the specific mechanical properties of the MBCC CCSs with different relative densities were narrower than the huge disparity among the mechanical properties, the CCSs still performed an increasing characteristic in the specific mechanical properties as the relative density increased. The increased relative density facilitated the mechanical properties and specific mechanical properties but lowered the light weight. In other words, the light weight and load-bearing capacity of the MBCC CCSs seemed to be contradictory. Achieving the light weight and extraordinary mechanical properties of the CCSs simultaneously is still a challenge.

The final states of the MBCC CCSs after testing were extremely beneficial to further understanding their behaviors under the compressive loading. It is concluded from Fig. 5 that, there were three fracture forms in the MBCC CCSs, containing lateral, vertical,

and inclined fractures. The fractures mainly originated from the pores and interfaces between the layers. Porosity of the additively manufactured bulk $Al_2O_3$ was 7.03%, meaning that some defects containing the pores and microcracks existed. In the loading process, the microcracks initiated from the micropores and easily merged with each other. The extended cracks resulted in the fracture of the struts in the inclined and vertical forms. Besides, the lateral fracture was attributed to the interfaces between the layers [33]. Extensive defects appeared on the interfaces between the layers after sintering, leading to weak interface strength [34]. Under the compressive loading, inclined struts in the CCSs tended to rotate around the joints. The rotating tendency tore the struts along the weak interface, making the appearance of the lateral fracture. Furthermore, as the relative density increased, the proportion of the inclined fracture dramatically decreased, which was perhaps attributed to the incrassated struts. The failure modes of the MBCC CCSs with two and three layers were consistent with that of the one-layer MBCC CCSs. That is to say, the increased relative density altered the failure mode of the MBCC CCSs, making it change from a parallel–vertical–inclined mixed mode to a parallel–vertical mode.

### 3. 3 Effect of layer

The stress–strain curves of the MBCC CCSs exhibited in Fig. 3 are rearranged in Fig. 6 to clear the effect of the layers on the mechanical properties of the CCSs. It is found in Fig. 6 that, no matter what the relative density was, the slopes, i.e., Young's modulus, of the stress–strain curves of the one-layer and two-layer MBCC CCSs were basically the same. However, the compressive strength of the one-layer MBCC CCSs was slightly higher than that of the MBCC CCSs with two layers. For instance, the average Young's moduli of O25 and T25 revealed in Fig. 4 are 0.14 and 0.14 GPa, respectively, and the average compressive strength of O25 was 5.16 MPa, slightly higher than that of T25 (4.07 MPa). Meanwhile, the Young's modulus of the three-layer MBCC CCSs was obviously greater than those of others. However, the compressive strength of the three-layer MBCC CCSs was not always the maximum. Furthermore, the energy absorption of the MBCC CCSs decreased as the layers increased because of the decreased strain. Significantly, the layers also affected the specific mechanical properties of the MBCC CCSs in the same way as that affected the mechanical properties, as illustrated in Fig. 4. Also, the gap between the specific mechanical properties of the CCSs with different layers also narrowed.

Besides, the exponents in Eq. (3), fitting the compressive strengths of the MBCC CCSs in Group O, Group T, and Group TH, are 2.37±0.18, 3.08±0.17, and

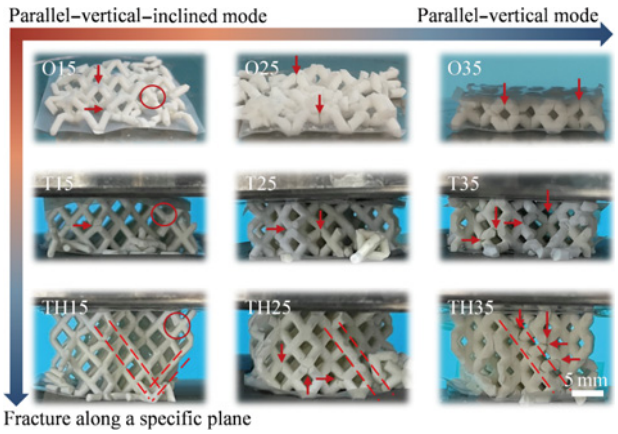


**Fig. 5** Final states of CCSs in Group O, Group T, and Group TH.

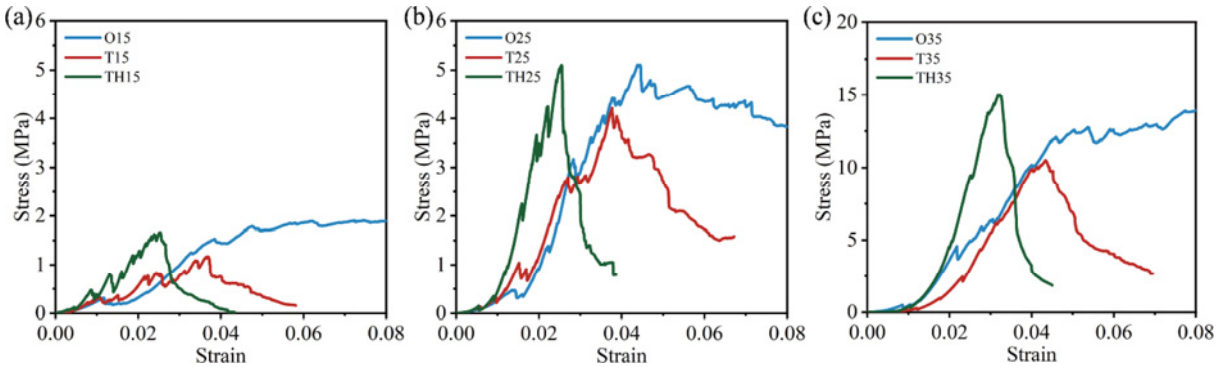


**Fig. 6** Representative compressive stress–strain curves of MBCC CCSs with different relative densities: (a) 15%, (b) 25%, and (c) 35%.

3.54±0.29, respectively. The exponents in Eq. (4) calculating the Young's moduli of the one-layer, two-layer, and three-layer MBCC CCSs are 3.04±0.49, 3.37±0.20, and 3.64±0.42, respectively. Eq. (5) is used for fitting the energy absorption of the MBCC CCSs with one, two, and three layers, and the exponents in Eq. (5) are 2.10±0.25, 3.61±0.44, and 3.80±0.28, respectively. Something interesting could be concluded that the exponents in Eqs. (3)–(5) increased as the layers increased. That is to say, the influence of the structural parameters on the mechanical properties of the CCSs was not independent, and they will be altered by each other. As the layers increased, the influence of the relative density on the mechanical properties, not only the compressive strength but also the Young's modulus and energy absorption, of the MBCC CCSs were magnified.

As mentioned in Section 3.2, the failure mode of the MBCC CCSs changed from the parallel–vertical–inclined mixed mode to the parallel–vertical mode as the relative density increased. The same thing happened on the CCSs with more layers. When the number of the layers increased to three, just part of the joints was destroyed instead of all joints. The broken joints tended to focus on a specific plane. The more layers, the more apparent this failure mode [16,26]. Because once the joints in the multi-layer MBCC CCSs were destroyed, the complete joints at neighboring were forced to share more loadings to make the CCSs stable again. Hence, the neighboring joints would get damaged earlier because of the higher force. In brief, the MBCC CCSs were inclined to fracture along a specific plane as the layers increased. That is to say, the inclined fracture took a greater proportion in the failure mode of the multi-layer CCSs. It was noteworthy that the incremental relative density would stop the transformation of the failure mode from the parallel– vertical–inclined mode to the fracture along a specific plane, leading to a decreased proportion of the inclined fracture.

### 3. 4 Effect of size

Here, we analyzed how the size of the unit cells influenced the mechanical properties of the CCSs combined with Ref. [33]. The designed sizes of the unit cells in Group O and Group H were 10 mm × 10 mm × 7.07 mm and 7.78 mm × 7.78 mm × 5.5 mm, respectively, i.e., narrowing the unit cells in Group O to 77.8% will obtain the unit cells in Group H. As depicted in Figs. 7(a) and 7(b), although the values exhibited in the stress–strain curves of the one-layer MBCC CCSs in Group O and Group H were different, there was great consistency in the morphologies of their stress–strain curves. Furthermore, the one-layer MBCC CCSs with a smaller dimension performed more outstanding mechanical properties and specific mechanical properties, as illustrated in Figs. 7(c)–7(h). The increasing compressive strength may be ascribed to the shortened length of the struts. The strains of the one-layer MBCC CCSs in Group O and Group H were basically the same. Thus, the energy absorption was mainly dependent on the compressive strength. Hence, the high-strength CCSs in Group H exhibited higher energy absorption ability [33]. It was surprisingly concluded that appropriately reducing the size of the unit cells could efficiently improve the mechanical properties without sacrificing the lightweight of the CCSs.

As revealed in Fig. 8, with the increase of the relative density, the failure mode of the one-layer MBCC CCSs in Group H changed from the parallel–vertical–inclined mixed mode to the parallel–vertical mode, agreed with that of the MBCC CCSs in Group O. That is to say, the failure mode of the CCSs was independent of the size of the unit cells.

### 3. 5 Effect of structural configuration

The structural configuration was proved to be a significant factor in altering the response of the cellular structures under the compressive loading [35]. Herein, we combined our work about the CCSs to analyze how the structural configurations influenced their mechanical properties [26]. The CCSs with the structural configurations of the BCC, Octet, MBCC, SchwarzP, and IWP, as depicted in Fig. 9(a), were fabricated to examine their mechanical properties. It is found in Figs. 9(b)–9(e) that the MBCC40 CCS had the highest compressive strength (23.90±2.74 MPa), followed by the Octet40 CCS (12.48±1.72 MPa), SchwarzP40 CCS stepped (10.58±0.76 MPa), and IWP40 CCS stepped (8.39±0.19 MPa); the BCC40 CCS was the poorest (6.72±0.66 MPa). The order of the Young's moduli from high to low was the MBCC40 CCS (2.73±0.01 GPa), Octet40 CCS (2.19±0.35 GPa), SchwarzP40 CCS (1.55±0.27 GPa), IWP40 CCS (1.02±0.06 GPa), and BCC40 CCS (0.97±0.26 GPa), which was consistent with that of the compressive strength [26]. That is to say,

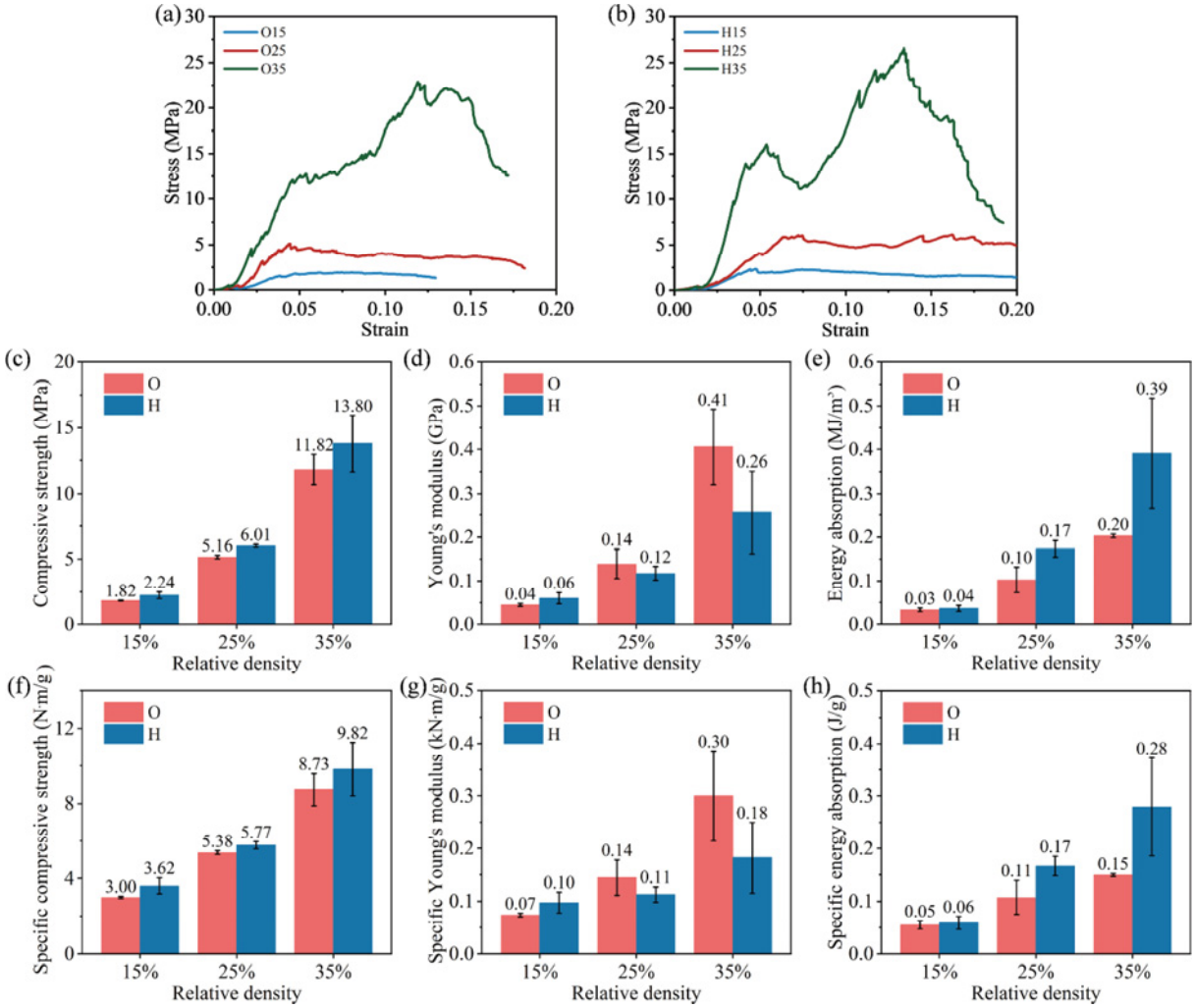


**Fig. 7** Stress–strain curves of one-layer MBCC CCSs in (a) Group O and (b) Group H. Comparison between mechanical properties of one-layer MBCC CCSs in Group O and Group H: (c) compressive strength, (d) Young's modulus, (e) energy absorption, (f) specific compressive strength, (g) specific Young's modulus, and (h) specific energy absorption.

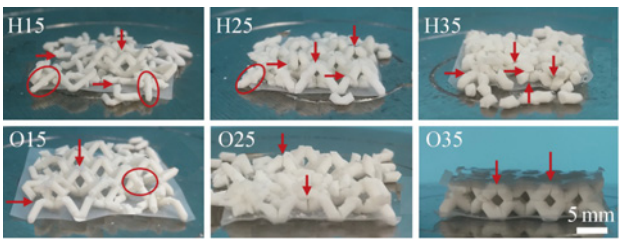


**Fig. 8** Final states of one-layer MBCC CCSs in Group O and Group H.

the mechanical properties of the CCSs were closely associated with their structural configurations. As a typical bending-dominated structure, the mechanical properties of the BCC40 CCS, without a doubt, were the poorest among those of the five CCSs [36]. The Octet was a representative stretching-dominated structure that had been extensively investigated. Of course, the mechanical properties of the Octet40 CCS were more outstanding than those of the BCC40 CCS. The MBCC structure was designed based on the BCC structure, aiming to alleviate the bending tendency of the struts [33]. It was expected that the MBCC40 CCS performed the most outstanding compressive strength and Young's modulus with the help of the decreased bending tendency and increased inclination angle of the struts [37,38]. Also, that was exactly what happened. The TPMS structures were introduced to alleviate the stress concentrated on the joints [39]. However, this was not the way that things turned out. The compressive strengths and Young's moduli of the SchwarzP40 and IWP40 CCSs were not superior to those of the MBCC40 CCS, just being intermediate between those of the Octet40 and BCC40 CCSs. The unexpected mechanical properties of the SchwarzP40 and IWP40 CCSs may be caused by the decreased thickness of walls. Besides, the

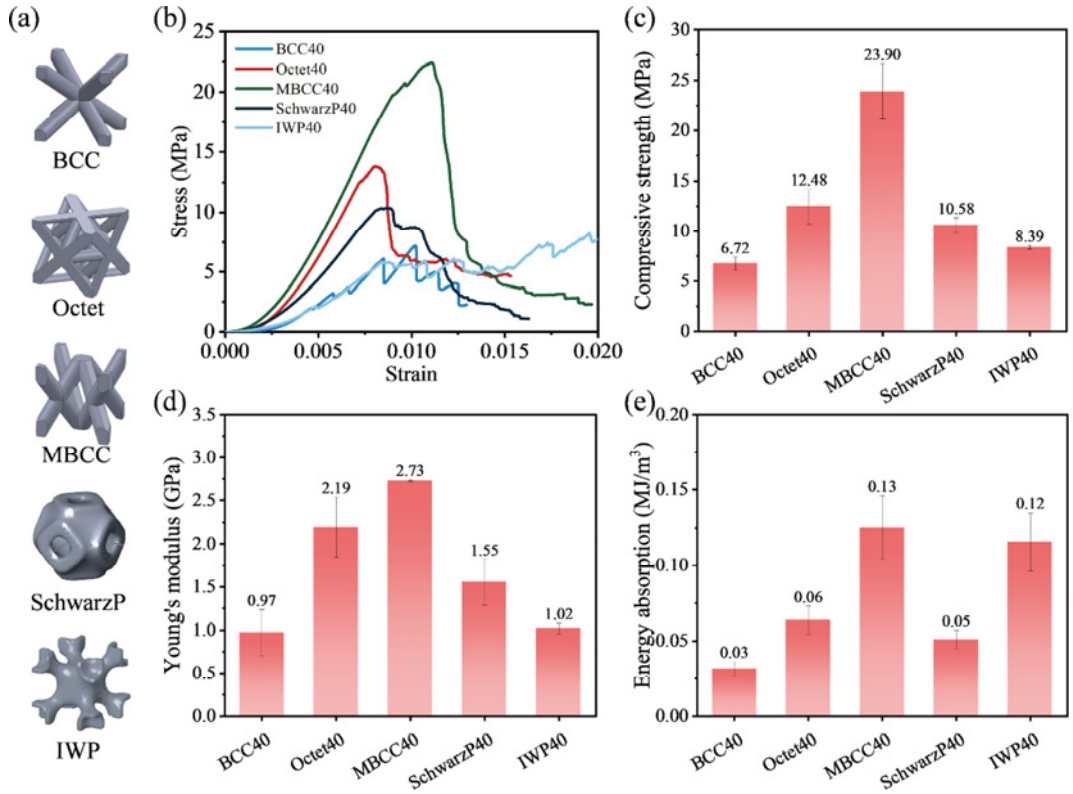


**Fig. 9** (a) Unit cell models of multi-layer CCSs. (b) Compressive stress–strain curves of CCSs in Group D. Summarization of mechanical properties of CCSs with different structural configurations: (c) compressive strength, (d) Young's modulus, and (e) energy absorption. Reproduced with permission from Ref. [1] for (a), © The Authors 2022.

theoretical ranking of the energy-absorbing ability of the CCSs should be consistent with those of the compressive strength and Young's modulus. However, the energy absorption of the IWP40 CCS (0.12±0.02 MJ/m$^3$) was distinguished, which was almost as high as that of the MBCC CCS (0.13±0.02 MJ/m$^3$). Because the as-prepared IWP40 CCS severely cracked along the interlayers resulting from their structural characteristic, as shown in Fig. 2. The existing cracks were gradually closed under the external loading by the progressive fractures. Although the compressive strength of the IWP40 CCS was comparatively lower, fundamentally the same as the compressive strength of the BCC40 CCS, its strain was much higher than those of others. Hence, the IWP40 CCS exhibited inferior compressive strength and Young's modulus but superior energy absorption. Because of the same relative density, i.e., 40%, the varying tendency of specific mechanical properties of the CCSs in Group D was the same as that of the mechanical properties. In a word, the structural configuration significantly influenced the responses of the CCSs under the compressive loading.

It was manifested in Section 3.3 that the CCSs are inclined to fracture along a specific plane as the layers increase. Meanwhile, the incremental relative density would decrease the proportion of the inclined fracture. Something changed when the structural configuration was taken into consideration. The BCC40, Octet40, MBCC40, SchwarzP40, and IWP40 CCSs had the same relative density and layer. However, there was a relatively large difference in their failure mode. For example, the BCC40 and Octet40 CCSs apparently fractured along a specific plane, whose inclined angle was closely related to the structural configuration. Nevertheless, the inclined fracture was not apparent in the final state of the MBCC40 CCS. The parallel–vertical mode was predominant. Of course, such failure mode happened on the CCSs with not only the lattice structures but also the TPMS structures. As illustrated in Fig. 10, the cracks in the SchwarzP40 CCS initiated from somewhere parallel and vertical to the loading direction. Although some interlayer cracks existed on the IWP40 CCS, most fractures still focused on a 45° plane. In a word, the structural configuration played a key role in the failure mode of the multi-layer CCSs [16].

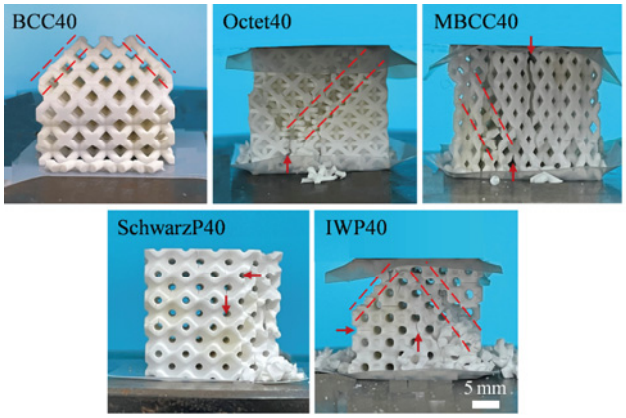


**Fig. 10** Final states of multi-layer CCSs with different structural configurations: (a) BCC40, (b) Octet40, (c) MBCC40, (d) SchwarzP40, and (e) IWP40.

## 4 Conclusions

The mechanical properties of the CCSs were essential for their application in aerospace and modern industry. Here, we systematically investigate the mechanical properties of the CCSs with distinct structural parameters. The conclusions obtained from this research, as visualized in Fig. 11, were listed as follows:

1) To systematically investigate the effect of the structural parameters on the mechanical properties of the CCSs under the compressive loading, the CCSs with different relative densities, layers, sizes, and structural configurations were prepared by the DLP-based AM technology in our works.

2) With the increase of the relative density, the mechanical properties and specific mechanical properties of the one-layer MBCC CCSs got apparently improved. The relationships between the mechanical properties and the relative density obeyed the exponential models. Besides, the failure mode of the MBCC CCS changed from a parallel–vertical–inclined mixed mode to a parallel–vertical mode with the increased relative density.

3) The compressive strengths and Young's moduli of the MBCC CCSs with one and two layers were basically the same, which were relatively lower than those of the MBCC CCSs with three layers. The energy absorption was the opposite. The same thing happened on the specific mechanical properties. Significantly, the increased layer amplified the effect of relative density. Besides, the MBCC CCSs were inclined to fracture along a specific plane as the layers increased, which was suppressed by the increased relative density to some extent.

4) The size of the unit cells did not affect the failure mode of the MBCC. However, the mechanical properties and specific mechanical properties of the CCSs were improved by shrinking the size of the unit cells. Shrinking the size while decreasing the relative density may be an effective method to keep the load-bearing capacity of the CCSs without sacrificing the light weight.

5) The mechanical properties of the multi-layer CCSs were hugely influenced by their structural configurations. The MBCC40 CCS had the highest compressive strength and Young's modulus, followed by the Octet40 CCS, SchwarzP40 CCS stepped, and

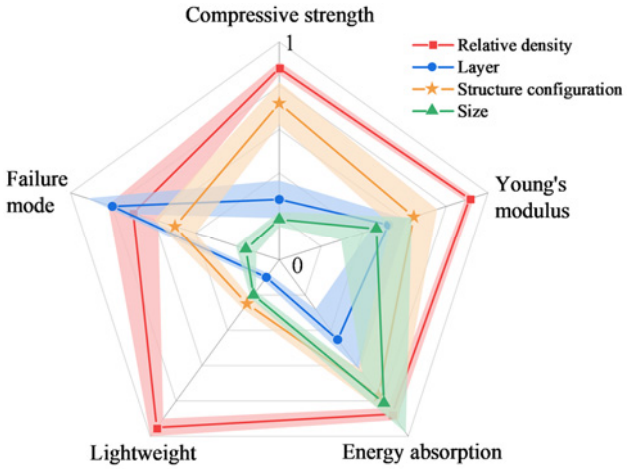


**Fig. 11** Influence of structural parameters on mechanical properties and failure mode of CCSs in a radar map. Except for failure mode, the values here were calculated by dividing the difference between maximum and minimum into the maximum. An example is given to calculate influence of relative density on mechanical properties of CCSs, which is represented by $A$ where A is defined as the influence factor, which represents the effect degree of each structural parameter on the mechanical and failure modes of the CCSs. Compressive strengths of O15, O25, and O35 are 1.82, 5.15, and 11.82 MPa, respectively. Compressive strengths of T15, T25, and T35 are 1.14, 4.07, and 11.23 MPa, respectively. Compressive strengths of TH15, TH25, and TH35 are 1.57, 5.01, and 14.96 MPa, respectively. $A$ is calculated by $(A_1+A_2+A_3)/3$, where $A_i$ is calculated by $A_i = (S_{\max} - S_{\min}) / S_{\max}$. That is to say, $A_1 = (S_{O35} - S_{O15}) / S_{O35} = 0.85$, $A_2 = (S_{T35} - S_{T15}) / S_{T35} = 0.90$, and $A_3 = (S_{TH35} - S_{TH15}) / S_{TH35} = 0.90$. Hence, $A = 0.88$, which exhibited a dot. Standard deviations of $A_1$, $A_2$, and $A_3$ represent the range of colorful error band around dots. Effect of structural parameters on failure mode was estimated by proportion of dot fracture along a specific plane. The greater the fracture along a specific plane was, the higher the value was.

IWP40 CCS stepped; the BCC40 CCS was the poorest one. The energy absorption of the IWP40 CCS was extremely high because of the existing fabricating interlayer cracks. The proportions of the parallel–vertical mode and fracture along a specific plane always changed with the variation of the structural configurations.

This study comprehensively concluded how the structural parameters acted in the mechanical properties and failure mode of the additively manufactured CCSs, which will serve as a foundation for investigating and designing the CCSs with the specific mechanical properties.

## Acknowledgements

This work was supported by the National Natural Science Foundation of China (Grant No. 51772028).

## Declaration of competing interest

The authors have no competing interests to declare that are relevant to the content of this article.

## References

[1] Zhang XQ, Zhang KQ, Zhang L, *et al*. Additive manufacturing of cellular ceramic structures: From structure to structure–function integration. *Mater Design* 2022, **215**: 110470.

[2] Wang WQ, Zhang L, Dong XJ, *et al*. Additive manufacturing of fiber reinforced ceramic matrix composites: Advances, challenges, and prospects. *Ceram Int* 2022, **48**: 19542–19556.

[3] Weeger O, Boddeti N, Yeung SK, *et al*. Digital design and nonlinear simulation for additive manufacturing of soft lattice structures. *Addit Manuf* 2019, **25**: 39–49.

[4] Feng CW, Zhang KQ, He RJ, *et al*. Additive manufacturing of hydroxyapatite bioceramic scaffolds: Dispersion, digital light processing, sintering, mechanical properties, and biocompatibility. *J Adv Ceram* 2020, **9**: 360–373.

[5] Schwarzer E, Holtzhausen S, Scheithauer U, *et al*. Process development for additive manufacturing of functionally graded alumina toughened zirconia components intended for medical implant application. *J Eur Ceram Soc* 2019, **39**: 522–530.

[6] Duan SY, Wen WB, Fang DN. Additively-manufactured anisotropic and isotropic 3D plate-lattice materials for enhanced mechanical performance: Simulations & experiments. *Acta Mater* 2020, **199**: 397–412.

[7] Feng YR, Guo X, Huang K, *et al*. Enhanced electromagnetic microwave absorption of SiOC ceramics targeting the integration of structure and function. *J Eur Ceram Soc* 2021, **41**: 6393–6405.

[8] Zheng HD, Liu LL, Deng CL, *et al*. Mechanical properties of AM $Ti_6Al_4V$ porous scaffolds with various cell structures. *Rare Metals* 2019, **38**: 561–570.

[9] Chen AN, Li M, Xu J, *et al*. High-porosity mullite ceramic foams prepared by selective laser sintering using fly ash hollow spheres as raw materials. *J Eur Ceram Soc* 2018, **38**: 4553–4559.

[10] Chen AN, Li M, Wu JM, *et al*. Enhancement mechanism of mechanical performance of highly porous mullite ceramics with bimodal pore structures prepared by selective laser sintering. *J Alloys Compd* 2019, **776**: 486–494.

[11] Yao YX, Qin W, Xing BH, *et al*. High performance hydroxyapatite ceramics and a triply periodic minimum surface structure fabricated by digital light processing 3D printing. *J Adv Ceram* 2021, **10**: 39–48.

[12] He RJ, Zhou NP, Zhang KQ, *et al*. Progress and challenges towards additive manufacturing of SiC ceramic. *J Adv Ceram* 2021, **10**: 637–674.

[13] Chen Z, Sun XH, Shang YP, *et al*. Dense ceramics with complex shape fabricated by 3D printing: A review. *J Adv Ceram* 2021, **10**: 195–218.

[14] Li CD, Gu HM, Wang W, *et al*. Microstructure and properties of Al–7Si–0.6Mg alloys with different Ti contents deposited by wire arc additive manufacturing. *Rare Metals* 2021, **40**: 2530–2537.

[15] Wang WQ, Bai XJ, Zhang L, *et al*. Additive manufacturing of Csf/SiC composites with high fiber content by direct ink writing and liquid silicon infiltration. *Ceram Int* 2022, **48**: 3895–3903.

[16] Mei H, Zhao RS, Xia YZ, *et al*. Ultrahigh strength printed ceramic lattices. *J Alloys Compd* 2019, **797**: 786–796.

[17] Gao SY, Wang C, Xing BH, *et al*. Experimental investigation on bending behaviour of $ZrO_2$ honeycomb sandwich structures prepared by DLP stereolithography. *Thin Wall Struct* 2020, **157**: 107099.

[18] Zhao WM, Wang C, Zhao Z. Bending strength of 3D-printed zirconia ceramic cellular structures. *IOP Conf Ser Mater Sci Eng* 2019, **678**: 012019.

[19] Brodnik NR, Schmidt J, Colombo P, *et al*. Analysis of multi-scale mechanical properties of ceramic trusses prepared from preceramic polymers. *Addit Manuf* 2020, **31**: 100957.

[20] Shen MH, Wang C, Zhao Z. Mechanical properties of $ZrO_2$ TPMS structures prepared by DLP 3D printing. *IOP Conf Ser Mater Sci Eng* 2019, **678**: 012017.

[21] Ashby MF. The properties of foams and lattices. *Phil Trans R Soc A* 2006, **364**: 15–30.

[22] Huang K, Elsayed H, Franchin G, *et al*. Additive manufacturing of SiOC scaffolds with tunable structure-performance relationship. *J Eur Ceram Soc* 2021, **41**: 7552–7559.

[23] Zhao WM, Wang C, Xing BH, *et al*. Mechanical properties of zirconia octet truss structures fabricated by DLP 3D printing. *Mater Res Express* 2020, **7**: 085201.

[24] Lu FL, Wu RH, Shen MD, *et al*. Rational design of bioceramic scaffolds with tuning pore geometry by stereolithography: Microstructure evaluation and mechanical evolution. *J Eur Ceram Soc* 2021, **41**: 1672–1682.

[25] Shuai XG, Zeng Y, Li PR, *et al*. Fabrication of fine and complex lattice structure $Al_2O_3$ ceramic by digital light processing 3D printing technology. *J Mater Sci* 2020, **55**: 6771–6782.

[26] Zhang XQ, Zhang KQ, Zhang B, *et al*. Quasi-static and dynamic mechanical properties of additively manufactured $Al_2O_3$ ceramic lattice structures: Effects of structural configuration. *Virtual Phys Prototy* 2022, **17**: 528–542.

[27] Vijayavenkataraman S, Kuan LY, Lu WF. 3D-printed ceramic triply periodic minimal surface structures for design of functionally graded bone implants. *Mater Design* 2020, **191**: 108602.

[28] AlMahri S, Santiago R, Lee DW, *et al*. Evaluation of the dynamic response of triply periodic minimal surfaces subjected to high strain-rate compression. *Addit Manuf* 2021, **46**: 102220.

[29] Zhang KQ, Xie C, Wang G, *et al*. High solid loading, low viscosity photosensitive $Al_2O_3$ slurry for stereolithography based additive manufacturing. *Ceram Int* 2019, **45**: 203–208.

[30] Zhang KQ, He RJ, Ding GJ, *et al*. Effects of fine grains and sintering additives on stereolithography additive manufactured $Al_2O_3$ ceramic. *Ceram Int* 2021, **47**: 2303–2310.

[31] He C, Ma C, Li XL, *et al*. Polymer-derived SiOC ceramic lattice with thick struts prepared by digital light processing. *Addit Manuf* 2020, **35**: 101366.

[32] Rasaki SA, Xiong DY, Xiong SF, *et al*. Photopolymerization-based additive manufacturing of ceramics: A systematic review. *J Adv Ceram* 2021, **10**: 442–471.

[33] Zhang XQ, Zhang KQ, Zhang B, *et al*. Additive manufacturing, quasi-static and dynamic compressive behaviours of ceramic lattice structures. *J Eur Ceram Soc* 2022, **42**: 7102–7112.

[34] Zhang KQ, Meng QY, Cai NJ, *et al*. Effects of solid loading on stereolithographic additive manufactured $ZrO_2$ ceramic: A quantitative defect study by X-ray computed tomography. *Ceram Int* 2021, **47**: 24353–24359.

[35] Kumar S, Ubaid J, Abishera R, *et al*. Tunable energy absorption characteristics of architected honeycombs enabled via additive manufacturing. *ACS Appl Mater Inter* 2019, **11**: 42549–42560.

[36] Deshpande VS, Ashby MF, Fleck NA. Foam topology: Bending versus stretching dominated architectures. *Acta Mater* 2001, **49**: 1035–1040.

[37] Huang YJ, Xue YY, Wang XF, *et al*. Effect of cross sectional shape of struts on the mechanical properties of aluminum based pyramidal lattice structures. *Mater Lett* 2017, **202**: 55–58.

[38] Huang YJ, Xue YY, Wang XF, *et al*. Mechanical behavior of three-dimensional pyramidal aluminum lattice materials. *Mater Sci Eng A* 2017, **696**: 520–528.

[39] Shen MH, Qin W, Xing BH, *et al*. Mechanical properties of 3D printed ceramic cellular materials with triply periodic minimal surface architectures. *J Eur Ceram Soc* 2021, **41**: 1481–1489.